Supplemental Figure Captions

Figure S1. Point spread function changes after pulse splitter installment, related to Figure 1.
(A) Imaging of a fluorescent bead (0.043 μm) in agar with and without pulse splitter installation shows a ~ 5.5-fold extension of the beam in the axial dimension with the lateral resolution unchanged.

Figure S2. Modulation of flux and diameter during resting state, related to Figure 1.
(A) Cross correlation analysis of diameter and RBC flux traces in wild-type mice, from data first reported in **Figure 1** (47 pial and penetrating arterioles). The distribution of maximum correlation values is shown on the left, with lag at maximum correlation plotted on the right. Only vessels with maximum correlation greater than 0.6 were included for lag time quantification. On average, RBC flux lags diameter by 0.16 seconds, a value which is statistically less than 0 ($p = 2x10^{-4}$, one-tailed t-test).
(B-G) Absolute changes in diameter and RBC flux during resting state vasomotion. All values were calculated using the fitting procedure shown in **Figures 1E,F**. Here we report changes in diameter Δd and changes in flux Δq before normalization by $\langle d \rangle$ and $\langle q \rangle$. Linear fits and corresponding R^2 values are given in the legends.
(B) PA diameter modulation versus average diameter.
(C) Pial arteriole diameter modulation versus average diameter.
(D) PA RBC flux modulation versus average diameter.
(E) Pial arteriole RBC flux modulation versus average diameter.
(F) PA RBC flux modulation versus average RBC flux.
(G) Pial arteriole RBC flux modulation versus average RBC flux.
(H) Arterial diameter modulation in the heart and breathing frequency ranges. Scatterplot of the root mean square diameter change, normalized by the average diameter, found
in the murine heart rate frequency range centered near 10 Hz and the breathing frequency range centered near 5 Hz; y axis versus arterial diameter x axis. These estimates are upper bounds, as all changes between 5 and 12 Hz were considered. The legend contains average ± SD values. Pial arteries are plotted as blue dots, penetrating arteries are plotted as orange stars. A two-sample KS test finds no significant difference between the pial and PA diameter modulation distributions ($p = 0.064$).

Figure S3. Change in flux through pial and penetrating arterioles during vibrissa stimulation, related to Figure 1.
(A) Joint distribution of the diameter versus the phase of the diameter of a pial artery during 0.1 Hz air puff stimulation of the vibrissa (3 mice, 17 pial arterioles, 13 penetrating arterioles). The median diameter in each phase bin is used to fit a function $\Delta d \cos \phi + \langle d \rangle$, where Δd is the

phase modulated amplitude, $\langle d \rangle$ is the baseline diameter and ϕ is the phase. The fitting has R^2 = 0.88 and normalized modulation depth $\Delta d/\langle d \rangle$ = 0.039. All error bars are the 25th and 75th percentiles.

(B) Joint distribution of the RBC flux versus the phase of the diameter of a pial artery during 0.1 Hz vibrissa air puff stimulation. The median flux in each phase bin is used to fit a function $\Delta q \cos \phi + \langle q \rangle$, where Δq is the phase modulated flux, $\langle q \rangle$ is the baseline flux and ϕ is the phase. The fit has R^2 = 0.89 and normalized modulation depth $\Delta q/\langle q \rangle$ = 0.051.

(C) Joint distribution of normalized change in flux ($\delta q/\langle q \rangle$) and normalized change in diameter ($\delta d/\langle d \rangle$). The median flux in each bin is used for a linear regression with R^2 = 0.98 and slope 1.22.

(D) Scatter plot of the diameter modulation depth versus variance explained by the phase modulation fitting illustrated in panel A. Pial and penetrating arteries are shown with color-coded average vessel diameter.

(E) Scatter plot of the flux modulation depth versus variance explained by the phase modulation fitting illustrated in panel B.

(F) Scatter plot of normalized flux-diameter slope, β, versus each slope's inverse variance weighting factor. Weighted averages yield β = 1.13 ± 0.22 and 1.31 ± 0.37 for the pial and penetrating arterioles respectively (mean ± SD, **Table 1**). The weighted average slope for pial arterioles is marked with a triangle.

Figure S4. Flux-diameter relationship during optogenetic arteriole constriction, related to Figure 1.

(A) Example 20 ms line scan images of vessel diameter (left) and RBC flux measurement (center) in PDGFRβ-cre x ReaChR mice (21 pial arterioles, 3 mice). To remove the vessel wall mCitrine background from flux measurement images the median intensity, over 20 ms, at every location across the vessel was subtracted (right).

(B) Time series of vessel diameter (blue) and RBC flux (orange) during the trial shown in (A). Inset: initial 20 percent decrease in diameter and corresponding RBC flux for this trial. The analogous 20 percent initial constrictions in each measured vessel were used for calculations in (C) and (D).

(C) Joint distribution of normalized change in RBC flux (δq/⟨q⟩) and normalized diameter change (δd/⟨d⟩) during initial 20 percent constrictions in all measured vessels. Red bars represent the median, 75th, and 25th percentile δq/⟨q⟩ in each δd/⟨d⟩ bin. A linear fit to all data yields β = 1.83 with R^2 = 0.93 (black line).

(D) Scatter plot of normalized flux-diameter slope, β, versus each slope's inverse variance weighting factor for each of the 21 pial arterioles. An inverse variance-weighted average yields β = 1.49 ± 0.90 (mean ± SD, **Table 1**), marked with a triangle. Average vessel diameters are represented by each point's color and are the average diameter during each vessel's initial 20 percent constriction.

Figure S5. Correlation between penetrating artery propagation direction measurements, related to Figure 2.
Pair-wise travel direction correlation as a function of distance between penetrating arteriole pairs. Within each distance bin, the average travel direction product is consistent with binomial sampling.

Figure S6. Resting state vascular calcium dynamics and example segmentations used to quantify GCaMP8.1 and jRGECO signals in wide-field analyses, related to Figures 3 and 4.
(A) Pial arteriole GCaMP8.1 and diameter spectra from two-photon extended beam measurements (27 pial arterioles, 837 locations, half bandwidth = 0.02 Hz). This dataset's acquisition and cross correlation analysis are illustrated in **Figure 3C,D**.
(B) Corresponding spectral coherence and phase between GCaMP8.1 and diameter signals at each location (27 pial arterioles, 837 locations, half bandwidth = 0.04 Hz). Spectra, coherence, and phase estimates are the average across all vessels, locations, and tapers. All error bars are 95% confidence intervals, calculated using leave-one location out jackknife estimates. Coherence is considered significant above the 0.95 confidence level; the estimate from two incoherent signals would exceed this in only 5 % of trials [1, 2].
(C) Neuronal and Vascular segmentation. An example smooth muscle GCaMP8.1 standard deviation mask, used to create the binary vessel mask (left). One example vessel with vessel segmentation and surrounding neural envelope (right). Each black or white pixel group identifies a computed vessel segment, over which vascular signals are averaged. The neuronal envelope is colored according to the distance from the initial vessel segment. GCaMP8.1 and neuronal jRGECO phase progressions for this example vessel, as a function of distance (bottom). Phase progressions are colored according to their corresponding segmentation above.

Figure S7. Inverse GRaFT predictions and GRaFT predictions during stimulation, related to Figure 6.
(A) Prediction of neural activity from vascular activity during rest.
(B) Prediction of neural activity from vascular activity during stimulation.
(C) Prediction of vascular activity from neural activity during stimulation. Stimulation trials consist of 500 second air puff and visual stimulation experiments.

Figure S8. Observed Ca^{2+} propagation speed in vessel segments of various lengths, related to Figure 7.
(A) An example pial vessel with non-monotonic phase progression. Previous quantification of Ca^{2+} propagation speeds in arteriole smooth muscle report a median speed of 0.97 mm/s, with an

interquartile range of 0.63 mm/s [3]. Munting et al. [3] used 510 x 510 um and 255 x 255 um fields of view. Using wide-field microscopy, we observe that Ca^{2+} phase progression is a non-monotonic function of distance on the millimeter scale. By recording short segments of this typical phase progression, one is biased toward larger $|\boldsymbol{k}|$ and therefore smaller speeds (blue random example fits with L = 0.3 mm, 0.01 significance level cutoff). To test if this could account for discrepancies in measured speed, given the intrinsic variability of phase progressions, we analyzed our wide-field dataset at various vessel segment lengths.

(B) Reanalysis of vasomotor wave propagation in the wide-field dataset at different vessel lengths. For each test length L, the full dataset was filtered to include only vessels longer than L. Then segments of length L were chosen from a random location within each larger vessel. Ca^{2+} wave speed was calculated for each shorter-length dataset by fitting the median f vs. $|\boldsymbol{k}|$, as described in the Methods, and was plotted in panel B. Blue points are plotted at the average length, with horizontal error bars as the full range of vessel segments used in each analysis and vertical error bars as the wave speed standard error. The black line represents the dataset used in this paper with lengths 0.75 mm to 3.5 mm, 1.2 ± 0.4 mm mean ± SD.

(C) Additional example phase progressions from the animal shown in **(A)**.

References

1. Jarvis, M.R. and P.P. Mitra, *Sampling properties of the spectrum and coherency of sequences of action potentials.* Neural Computation, 2001. **13**:717-749.
2. Hannan, E.J., *Multiple Time Series*. 1970, New York: Wiley.
3. Munting, L.P., O. Bonnar, M.G. Kozberg, C.A. Auger, L. Hirschler, S.S. Hou, S.M. Greenberg, B.J. Bacskai, and S.J. van Veluw, *Spontaneous vasomotion propagates along pial arterioles in the awake mouse brain like stimulus-evoked vascular reactivity.* Journal of Cerebral Blood Flow & Metabolism, 2023. **43**:1752-1763.

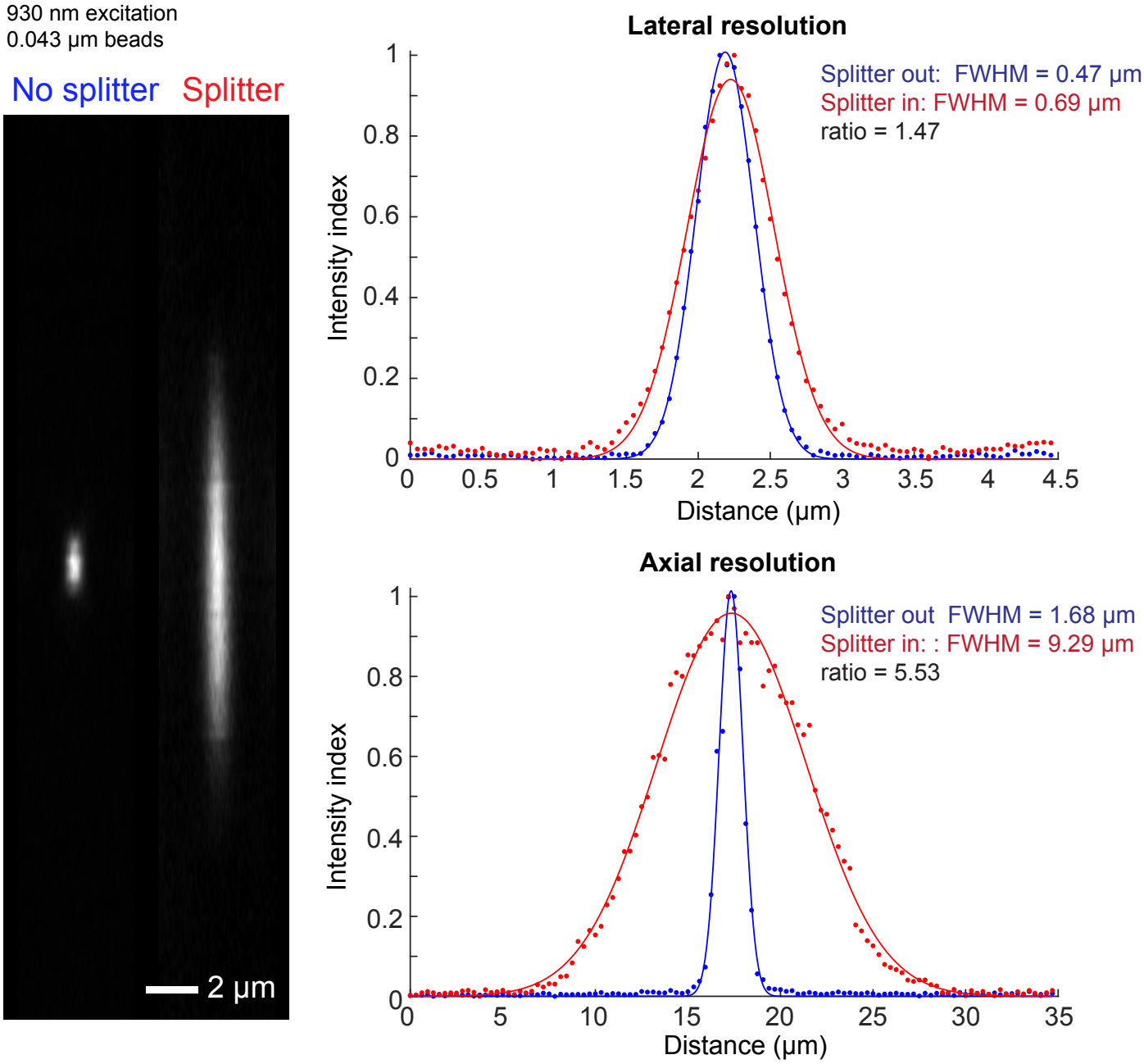

Figure S1. Broggini, Duckworth, Ji, Liu, Xia, Machler, Shaked, Munting, Iyengar, Kotlikoff, van Veluw, Vergassola, Mishne and Kleinfeld

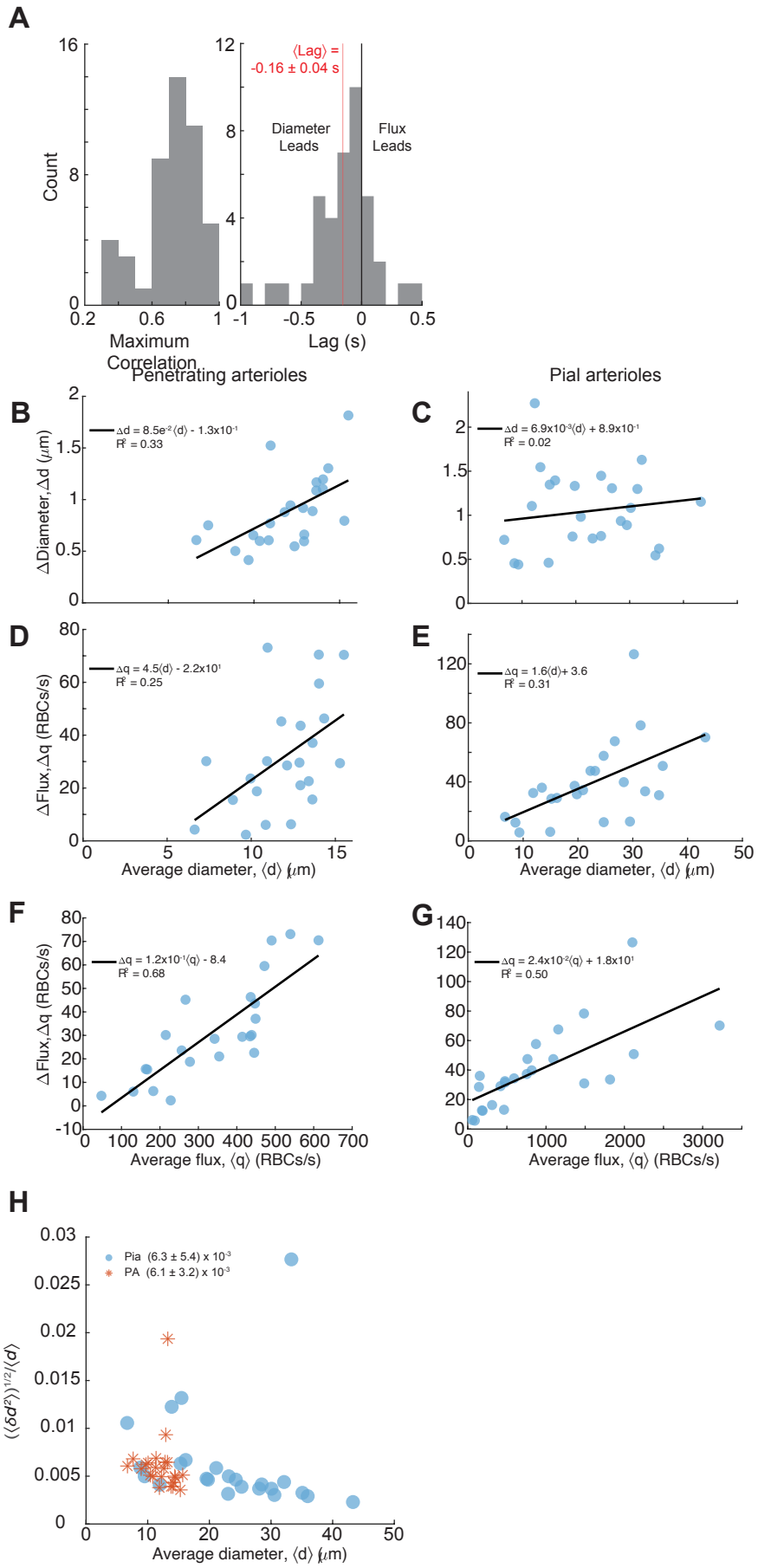

Figure S2. Broggini, Duckworth, Ji, Liu, Xia, Machler, Shaked, Munting, Iyengar, Kotlikoff, van Veluw, Vergassola, Mishne and Kleinfeld

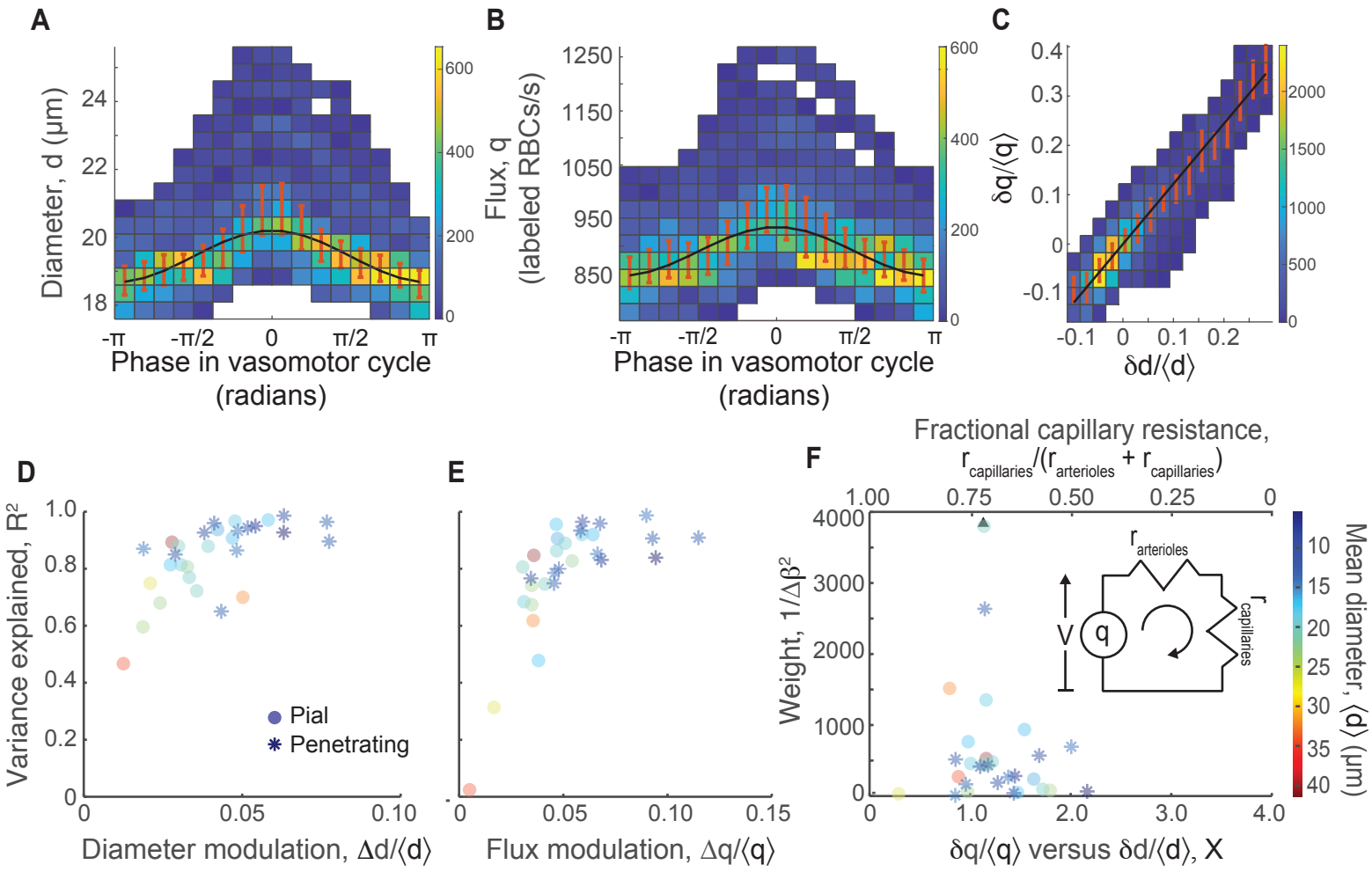

Figure S3. Broggini, Duckworth, Ji, Liu, Xia, Machler, Shaked, Munting, Iyengar, Kotlikoff, van Veluw, Vergassola, Mishne and Kleinfeld

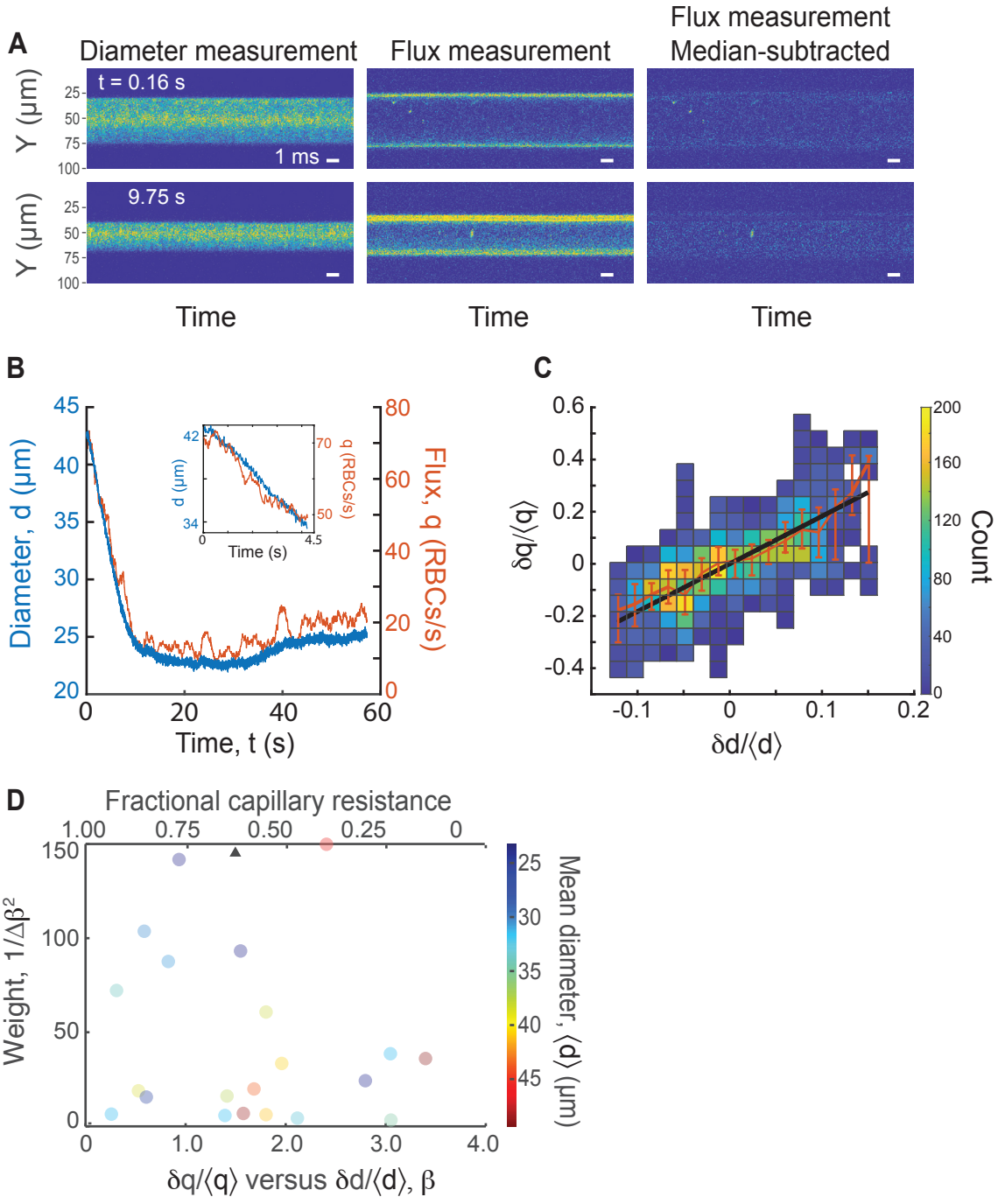

Figure S4. Broggini, Duckworth, Ji, Liu, Xia, Machler, Shaked, Munting, Iyengar, Kotlikoff, van Veluw, Vergassola, Mishne and Kleinfeld

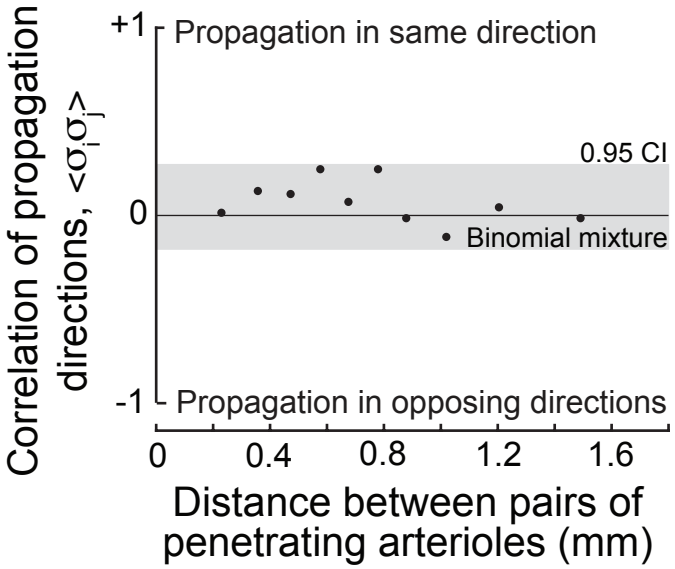

Figure S5. Broggini, Duckworth, Ji, Liu, Xia, Machler, Shaked, Munting, Iyengar, Kotlikoff, van Veluw, Vergassola, Mishne and Kleinfeld

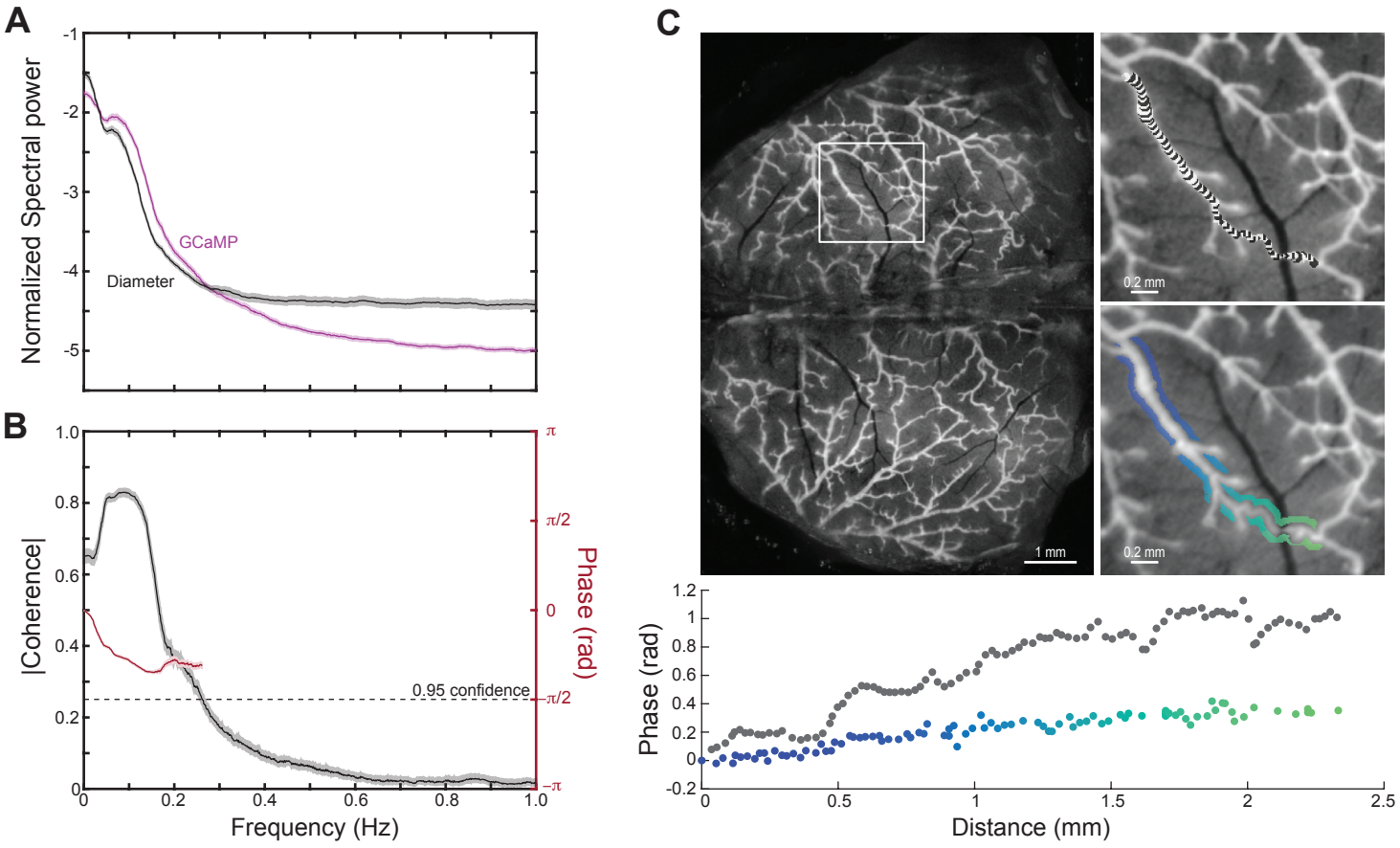

Figure S6. Broggini, Duckworth, Ji, Liu, Xia, Machler, Shaked, Munting, Iyengar, Kotlikoff, van Veluw, Vergassola, Mishne and Kleinfeld

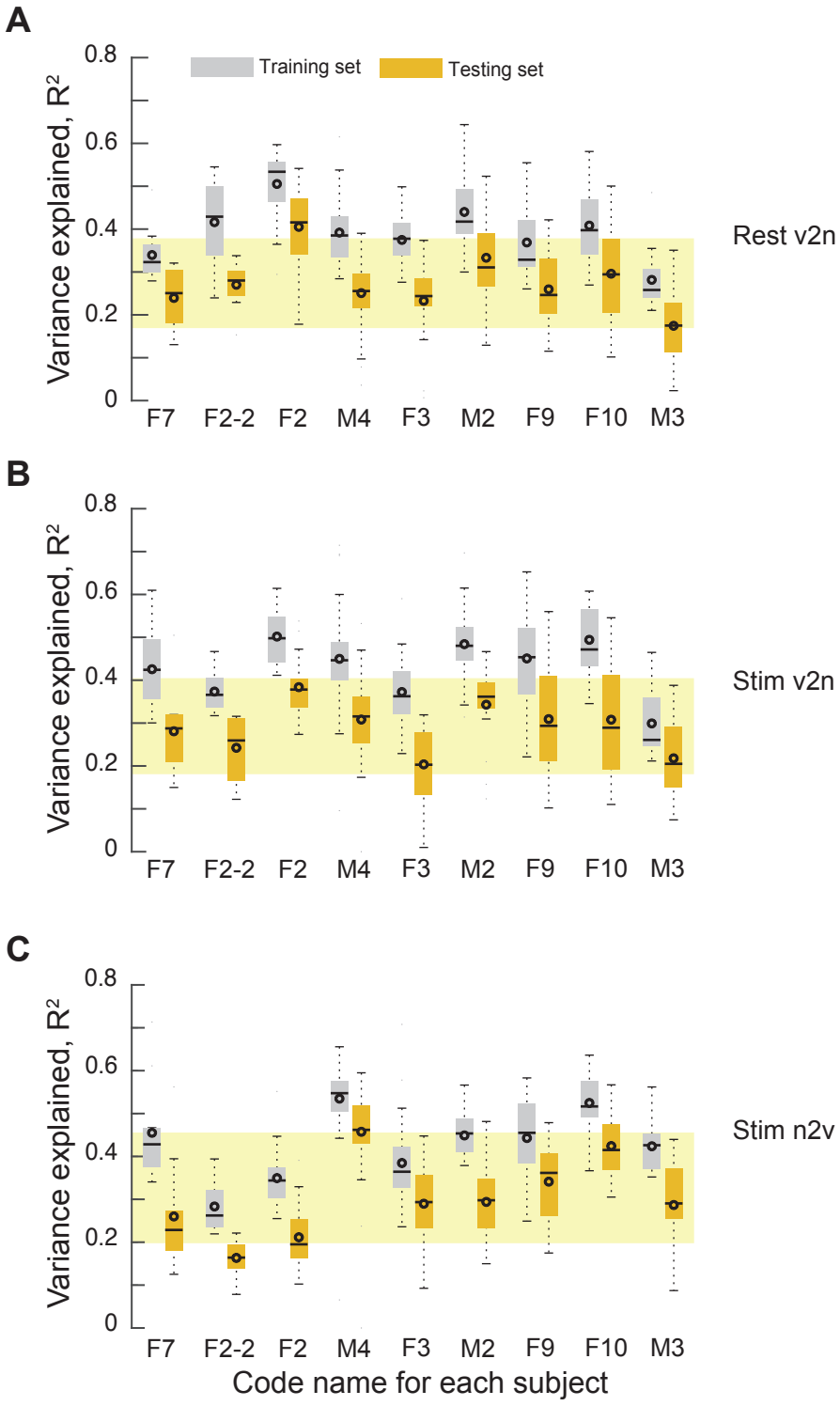

Figure S7. Broggini, Duckworth, Ji, Liu, Xia, Machler, Shaked, Munting, Iyengar, Kotlikoff, van Veluw, Vergassola, Mishne and Kleinfeld

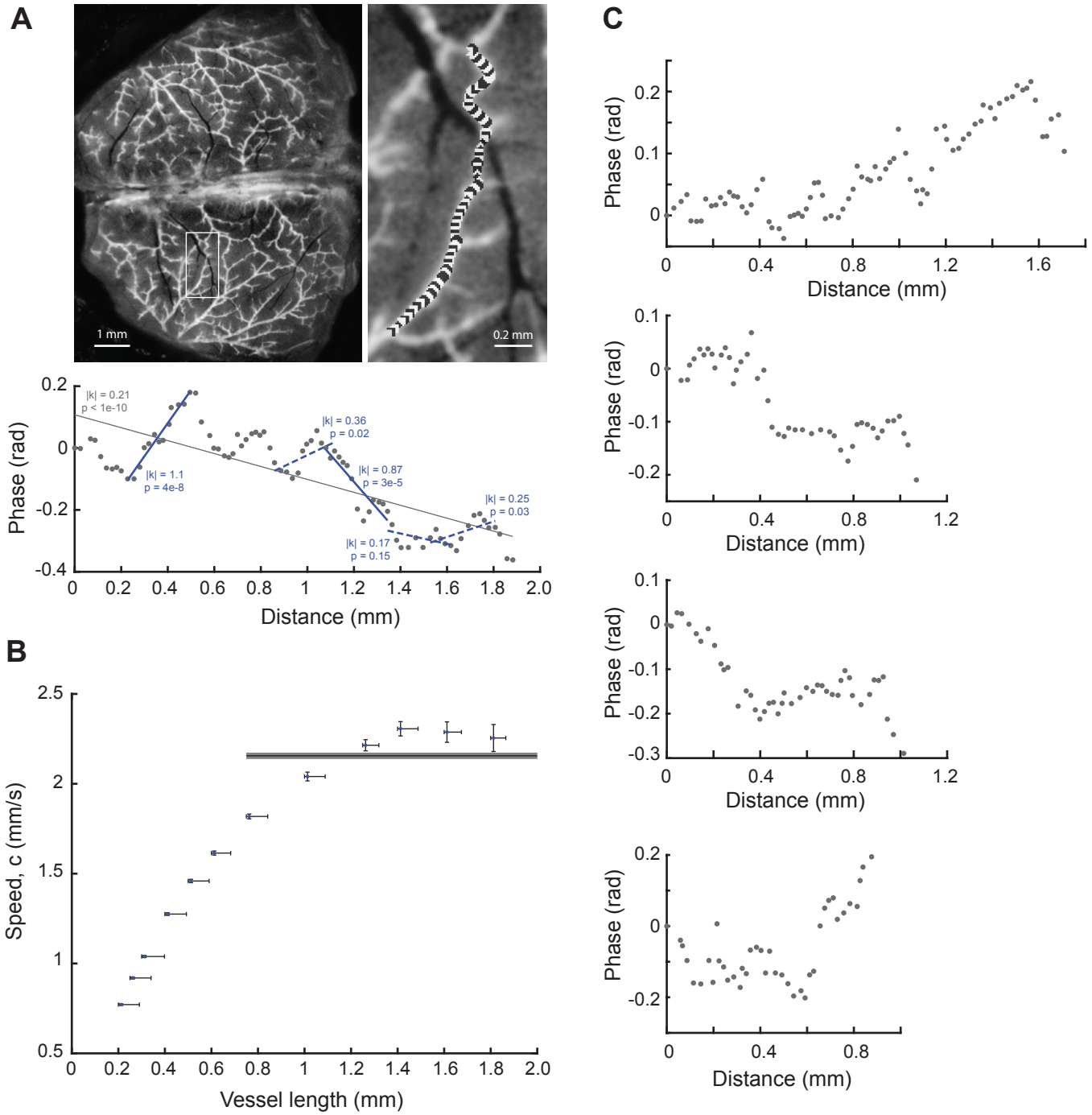

Figure S8. Broggini, Duckworth, Ji, Liu, Xia, Machler, Shaked, Munting, Iyengar, Kotlikoff, van Veluw, Vergassola, Mishne and Kleinfeld